Sparse sampling for fast quasiparticle-interference mapping

Oppliger, Jens ; Natterer, Fabian Donat

Abstract: Scanning tunneling microscopy (STM) is a notoriously slow technique; data-recording is serial, which renders complex measurement tasks, such as quasiparticle interference (QPI) mapping, impractical. However, QPI could provide insight into band-structure details of quantum materials that can be inaccessible to angle-resolved photoemission spectroscopy. Here we use compressed sensing (CS) to fundamentally speed-up QPI mapping. We reliably recover the QPI information from a fraction of the usual local density of state measurements. The requirement of CS is naturally fulfilled for QPI, since CS relies on sparsity in a vector domain, here given by few nonzero coefficients in Fourier space. We exemplify CS on a simulated Cu(111) surface using random sampling of uniform and varying probability density. The latter improves QPI recovery and mitigates Fourier artifacts. We further simplify the motion of the STM tip through an open traveling salesman's problem for greater efficiency and use the tip-path for drift correction. We expect that the implications of our CS approach will be transformative for the exploration of two-dimensional quantum materials.

DOI: https://doi.org/10.1103/physrevresearch.2.023117

Sparse sampling for fast quasiparticle-interference mapping

Jens Oppliger and Fabian Donat Natterer*
Department of Physics, University of Zurich, CH-8057 Zurich, Switzerland

(Received 18 November 2019; accepted 31 March 2020; published 1 May 2020)

Scanning tunneling microscopy (STM) is a notoriously slow technique; data-recording is serial, which renders complex measurement tasks, such as quasiparticle interference (QPI) mapping, impractical. However, QPI could provide insight into band-structure details of quantum materials that can be inaccessible to angle-resolved photoemission spectroscopy. Here we use compressed sensing (CS) to fundamentally speed-up QPI mapping. We reliably recover the QPI information from a fraction of the usual local density of state measurements. The requirement of CS is naturally fulfilled for QPI, since CS relies on sparsity in a vector domain, here given by few nonzero coefficients in Fourier space. We exemplify CS on a simulated Cu(111) surface using random sampling of uniform and varying probability density. The latter improves QPI recovery and mitigates Fourier artifacts. We further simplify the motion of the STM tip through an open traveling salesman's problem for greater efficiency and use the tip-path for drift correction. We expect that the implications of our CS approach will be transformative for the exploration of two-dimensional quantum materials.

DOI: 10.1103/PhysRevResearch.2.023117

I. INTRODUCTION

The saying *time is of the essence* also applies to the study of condensed matter systems, especially when experimental discovery trails the theoretical prediction of quantum materials [1–3]. This paradigm of *theory leading experiment* has made an important showing for topological insulators [4] and most recently in twisted van der Waals materials [5]. The ever-growing list of predicted candidate systems needs a matching effort to verify their properties.

Recent work has made meaningful strides at the higher level of feature analysis using machine learning [6], while the preceding data recording oftentimes remains on the sideline. Angle-resolved photoemission spectroscopy (ARPES) [7–9] has hereby served as the prime tool for band-structure investigations, routinely providing valuable insight into the electronic structure of candidate materials. However, the study of advanced materials also requires the preparation of conditions in which ARPES is inhibited. These limitations are particularly concerning in the view of micron-sized samples, field-effect devices, magnetic fields, cryogenic temperatures, and hole doped systems; all of which could trigger quantum phase transitions and that are natural control knobs in the exploration of quantum materials. Fortunately, a scanning tunneling microscope (STM) excels under these conditions. An STM is naturally surface sensitive, operates down to milli-Kelvin temperatures [10,11] at microelectronvolt energy resolution, in high magnetic fields, and on gate tunable devices. The STM obtains in-plane momentum sensitivity through the elastic scattering of electrons at surface discontinuities (such as atomic steps and point defects) that modulate the local density of states (LDOS) [12–14], which resemble standing wave patterns. These LDOS modulations provide access to the scattering space (q space) [15,16] via the Fourier transform, from which momentum space information can be inferred (k space). The band-structure mapping from LDOS modulations is known as Fourier-transform or quasiparticle interference (QPI) STM. Although QPI-STM appears viable for band structure determination, it presently is also excruciatingly slow, rendering the comprehensive study of a larger parameter space (temperature, magnetic field, doping, energy) cumbersome.

II. COMPRESSED SENSING FOR QPI RECOVERY

The throughput of a QPI investigation is presently constrained by the following considerations: In order to distinguish nuances in reciprocal space, the finest momentum space resolution of $q_{\mathrm{min}} = 2\pi/L$, where L stands for the physical size of the LDOS map, as well as a large number n of its increments, is desired. However, the total number N of point spectra that are used to map the LDOS(x, y, E) grows quadratically with the grid size $N = n \times n$, which quickly amounts to hundreds of thousands of spectra and daylong measurements [17], during which the experiment hinges at the mercy of a notoriously unpredictable STM tip.

Despite these measurement efforts, the resulting QPI patterns contain only a few nonzero coefficients as can be seen in Fig. 1 and previous work [6,14–16,18–33], suggesting a high degree of redundancy in conventional QPI mapping. Pointing out the undeniable sparsity in the QPI [33] pattern reveals an important connection to the key requirement of compressive sensing (CS) [34–36]. CS uses sparsity of information in some

*Author to whom all correspondence shall be addressed: fabian.natterer@uzh.ch

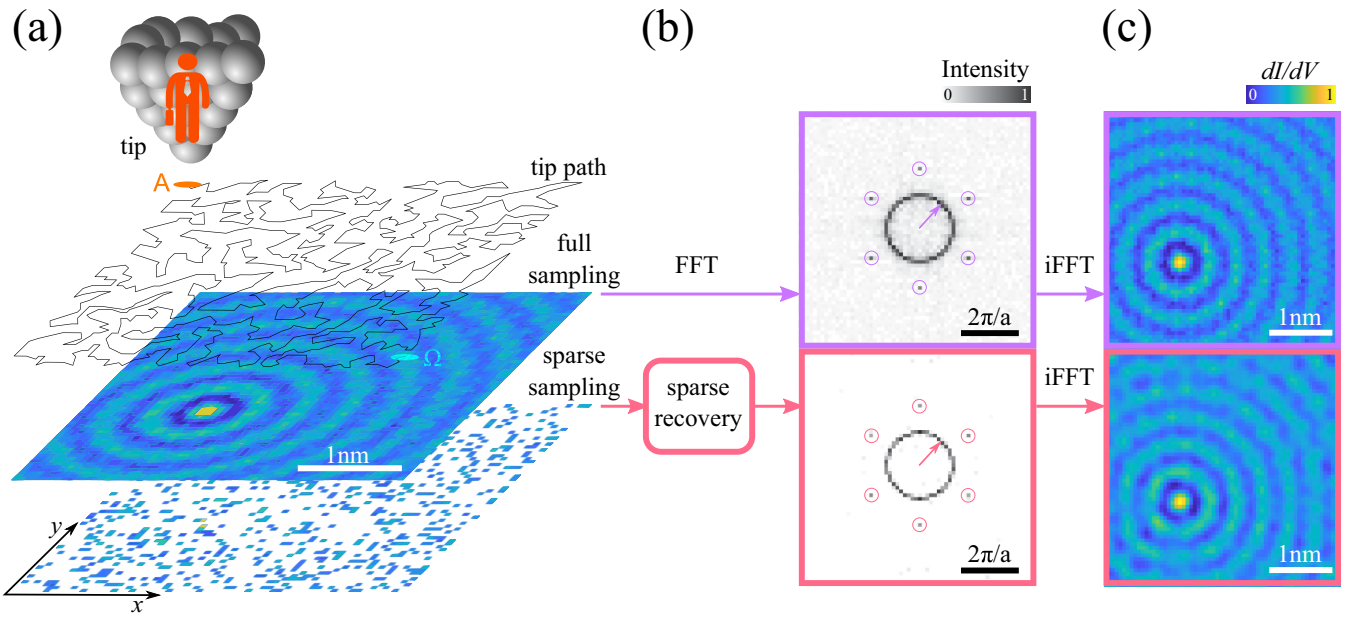

FIG. 1. Demonstrating the sparse sampling for quasiparticle interference mapping. (a) In conventional QPI mapping, the scanning tunneling microscope (STM) records the local density of state (LDOS) modulations on every surface point, here on a 64×64 grid of a simulated Cu(111) surface at ∼4.3 eV with an added Gaussian noise of 0.2 times the LDOS standard deviation. Using a sparse-sampling method, we only sample a small fraction of the full LDOS (here 20%) by efficiently moving the tip according to a traveling salesman between the distributed measurement locations. (b) The QPI pattern is the Fourier transform of the LDOS modulations as shown for the fully sampled LDOS of the conventional method (top) and from our 20% sparsely sampled LDOS (bottom). The wave vector of the surface state as well as the Bragg peaks of the Cu(111) lattice are identical in the original and recovered QPI pattern. (c) The QPI pattern allows the illustration of the original LDOS modulations via inverse Fourier transform, showing the excellent recovery and noise rejection for the sparsely sampled mapping.

vector representation and incoherent sampling to enable a data recording paradigm that requires radically fewer measurements than conventional sampling in the Nyquist regime. A suitable analogy for the present QPI case would be the sparse sampling of a sine wave in time domain (mimicking spatial LDOS modulations) and its CS recovery of the only two coefficients in Fourier space (equivalent to the sparse QPI pattern).

In the following, we exploit the sparsity of the QPI pattern to fundamentally speed up QPI mapping using a compressed sensing approach that we combine with an efficient STM tip-routing between randomly located LDOS measurements. Although the *posteriori* applicability of CS for STM measurements has been indicated before, it remained open how CS would be used for actual data taking [33].

Figure 1 exemplifies the difference between conventional QPI mapping and our compressed sensing method on a deliberately small $N = 64\times64$ grid for better visualization. The simulated copper surface state, generated by a Bessel function of the first kind [15], shows a standing wave pattern from an individual point scatterer that modulates the LDOS(x, y, E) and that we further perturb by additive white noise. From the fully sampled LDOS (conventional QPI), the Fourier transform produces the QPI pattern showing a ring of radius $q = 2k$ and six Bragg spots corresponding to the Cu(111) lattice. In perfect agreement, we recover the same QPI pattern from the sparsely sampled LDOS, seen in Fig. 1, using only 20% of random LDOS measurements. We obtain the original LDOS by an inverse Fourier transform of the recovered QPI in Fig. 1(c), which highlights the excellent CS reconstruction and complimentary noise rejection. Note that our CS method does not depend on a causal relationship between any two wave vectors but only on sufficient sparsity s in the Fourier domain (number of nonzero wave vectors vs number of possible wave vectors), where the condition for successful recovery is governed by the relationship between sparsity s and number of required measurements, as described in Appendix A and Ref. [36].

III. TRAVELING SALESMAN MEASUREMENT PATH

Since the locations at which we randomly measure the LDOS have to be visited by the STM tip, we interpret the path of the STM tip between those points as an open traveling salesman's problem (TSP) to save time and for which we find a near-optimal solution using a genetic algorithm [37]. Figure 1(a) shows an example of a near-optimal tip-path. The TSP further introduces a useful time correlation in the sampling data that we use to correct for drift in Sec. IV. Overall, this simple example reveals the fundamental time-savings of our CS method at a fivefold advantage compared to conventional QPI mapping, while the TSP optimized STM tip-path reduces the travel distance and time associated with the tip motion in that example by another ∼63% with respect to the fully sampled case.

We next unleash the working principle of our compressed sensing method onto a situation for which conventional QPI mapping is extremely challenging and that serves to illustrate

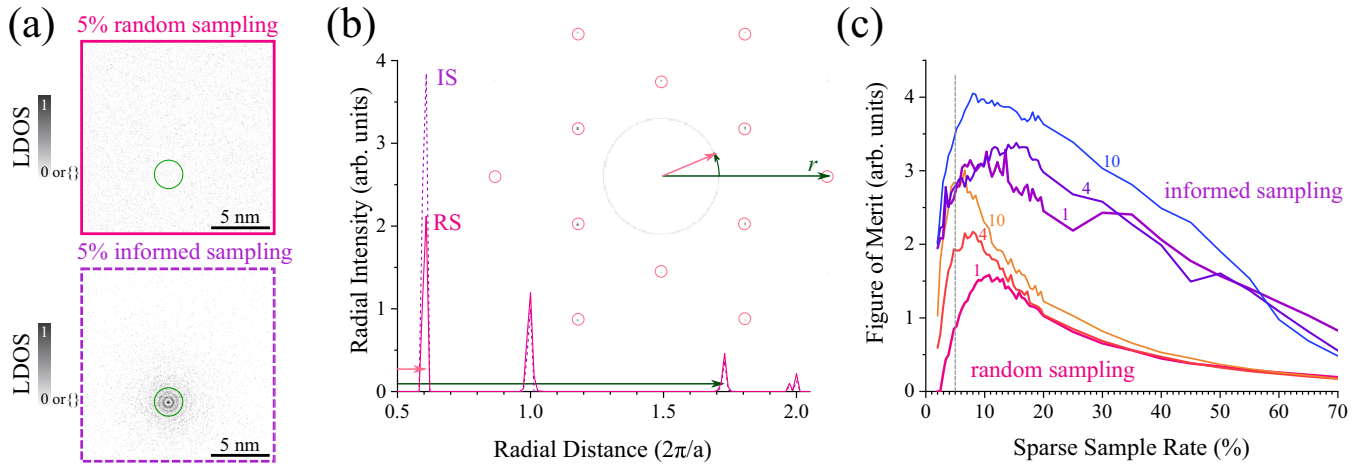

FIG. 2. Sparse sampling using random and informed probability densities. (a) Random (RS) and informed sampling (IS) of the LDOS modulations around a single point scatterer, calculated for ∼4.7 eV. Whereas the measurement locations in the former are chosen from a uniform probability density, they are concentrated around strong scatterers in the informed sampling case, leading to a denser pattern visible in the lower sampling mask. (b) Radial intensity profile of recovered QPI pattern using RS and IS sampling for 5% sampling rate and a 1-point scatterer. Both faithfully recover the QPI information and show the Cu surface state wave vector and Bragg peaks (inset). (c) Figure of Merit $\varphi = (A_{\text{peak}} \times C_{\text{ratio}})/\text{Full width at half maximum (FWHM)}$ comparison for RS and IS in dependence of the number of point scatterers (1,4,10). A_{peak} is the peak intensity of the QPI wave vectors and FWHM is seen in (b). C_{ratio} is the ratio of recovered coefficients with correct wavelength vs coefficients with wrong length. Informed sampling has an advantage over RS, especially for few point scatterers and low sampling density but tends towards RS at increasing number of point scatterers and sampling rate.

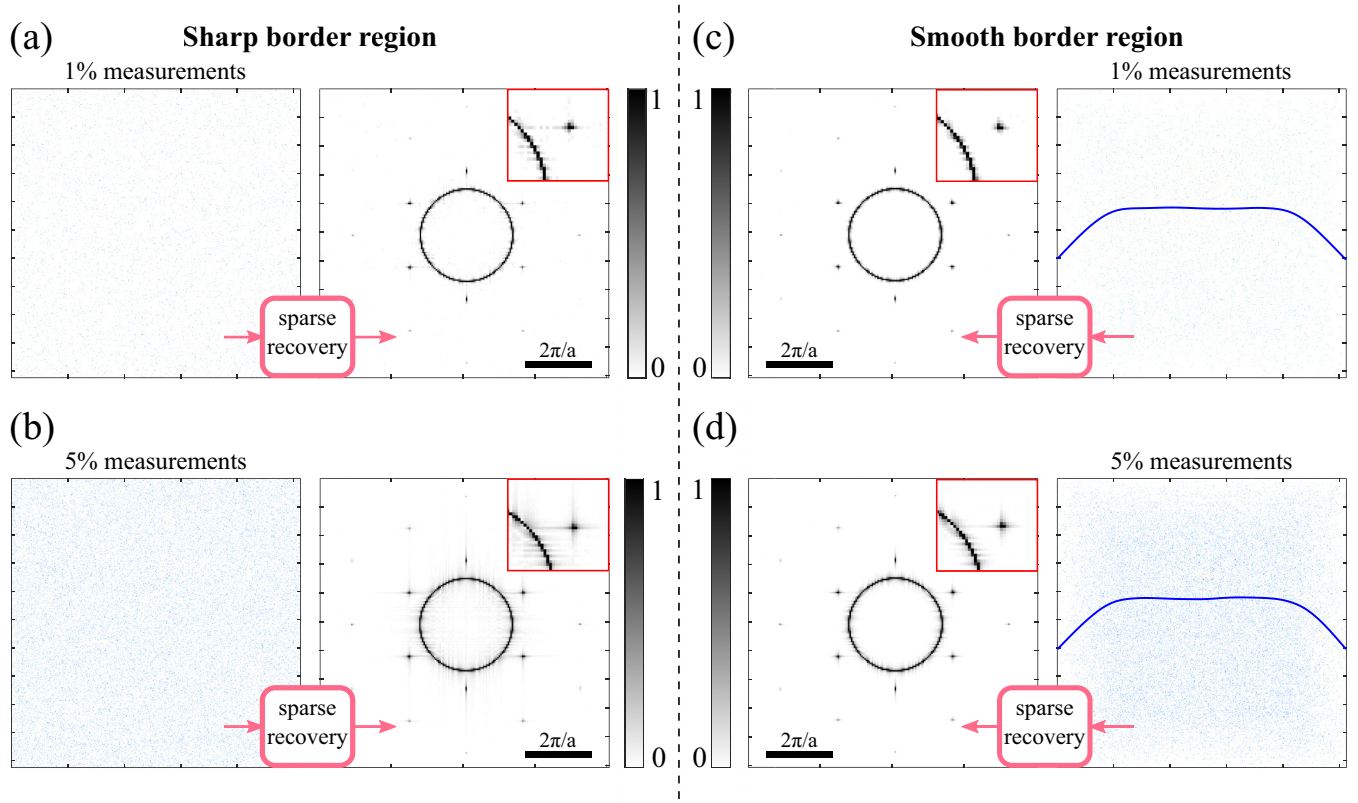

FIG. 3. Informed sampling variant to create FFT window functions. (a), (b) Regular random sampling mask (left) and QPI recovery (right) using 1 and 5% subsampling. The recovered QPI pattern is shown with a zoom to highlight the FFT artefacts. (c), (d) A nonuniform sampling mask using less measurement locations at the borders mitigates finite size effects that occur from the FFT transform. The streaks in the QPI pattern become suppressed, which improves assignment of QPI wave vectors. For both the RS and IS variant, we used the same LDOS, simulated on Cu(111) with 1-point scatterer at ∼6.5 eV on a 1024×1024 grid. The solid line in the right panels indicates the sampling density across the image frame.

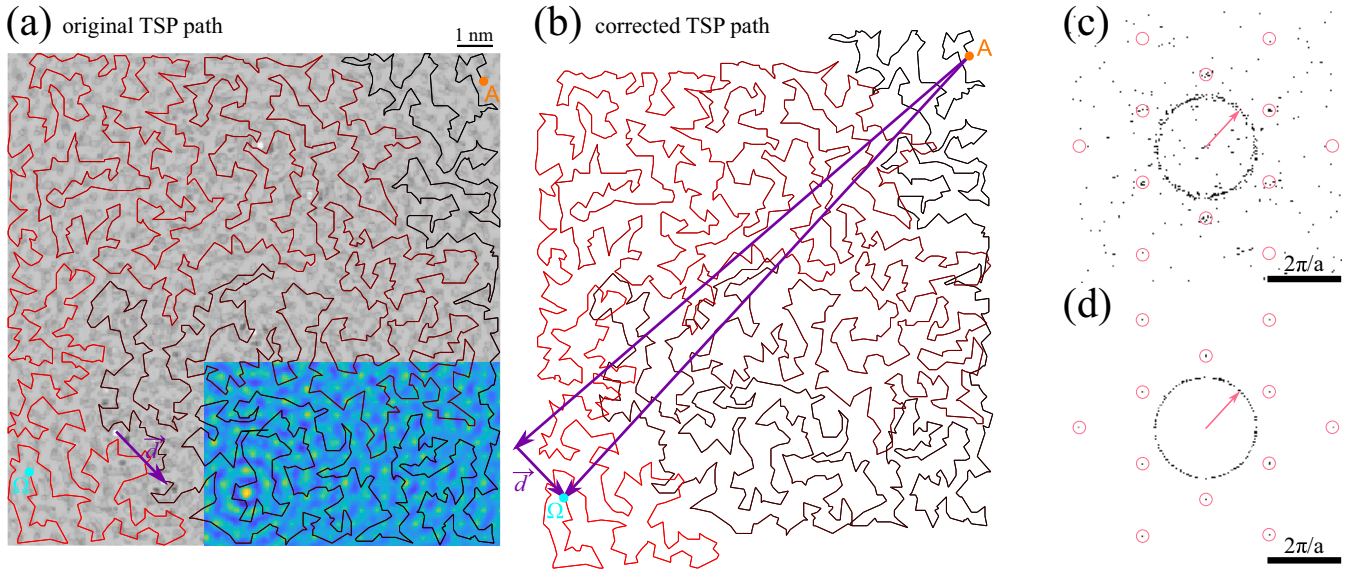

FIG. 4. Drift correction for sparsely sampled QPI. (a) Difference of LDOS measurements (grey) before and after sparsely sampled measurements, overlaid with planned TSP tip-path (the black-red gradient line connects starting point A and end point Ω). The bluish inset in the bottom right is the LDOS before TSP mapping. The LDOS was sparsely subsampled at 3% on a 256×256 grid. (b) An assumed drift $\vec{d}$ of about 15% with respect to the grid dimension leads to a repositioning of the effective LDOS locations, which we compensate by a reassignment of new coordinates. The long purple vectors connect A and Ω from the original and corrected TSP paths, showing that their difference exactly matches the drift vector $\vec{d}$. (c), (d) Comparison of QPI patterns obtained without and with drift correction, clearly showing the improved quality of the QPI pattern for the drift-corrected case, with higher-order Bragg peaks becoming visible. The surface state and the Bragg peaks are indicated by an arrow and circles in both QPI patterns.

the potential for quantum materials exploration. Figure 2(a) shows two sampling masks on a grid of size $N = 512\times512$, which we sparsely sample using only 5% of the LDOS data and for which we compare two sampling modalities. In the first, we apply regular random sampling (RS) with uniform sampling density, as explained before [Fig. 2(a) top panel]. In the second, we use informed sampling (IS) in which we accumulate more LDOS measurements with a probability density that follows a Lorentzian profile centered around known scattering sites. This sampling variant is motivated by the observation of dominant LDOS modulations in the immediate vicinity of surface discontinuities, such as step edges and point scatterers [12] [cf. Fig. 1(a)], whose intensities rapidly decay into the noise at increasing distance. Since these scattering sites are well-known from explorative topographies that typically precede QPI measurements, we specifically mark their (x, y) locations [green circle in Fig. 2(a)] around which we enforce a denser but still random sampling mask. From the comparison of the radial profile in Fig. 2(b), the advantage of IS compared to RS is visible, which would enable an even more reduced overall subsampling rate for faster QPI mapping. Although the advantage of IS slowly fades with increasing number of point scatterers [see Fig. 2(c)], it generally performs better than RS over the full range of subsampling fractions. Note that the figure-of-merit peaks once the majority of the wave vectors have been recovered and shrinks as an increasing number of false positives broaden the wave vectors due to fast-Fourier transform (FFT) related finite size effects.

In addition, IS offers efficiency opportunities for complementary scenarios in which regions are avoided instead of being sampled more densely. This could be required to exclude the influence of step-edges [17] to mask point impurities [32] that provoke tip-instabilities or to avoid point scatterers that may lead to unwanted LDOS modulations. The latter would have to be scrutinized by the experimenter prior to deciding which point scatterers merit their denser sampling. More importantly, our IS sampling modality offers further possibilities, such as the generation of windowing functions that limit the previously mentioned FFT artefacts. In order to illustrate this concept, we compare regular RS with IS of less densely sampled border regions with a linear gradient at the borders and a plateau in the center. Figure 3 demonstrates how the latter method mitigates FFT artifacts. The implementation of more sophisticated windowing functions is straightforward.

IV. LINEAR DRIFT CORRECTION

For a proper functioning of our compressed sensing approach, we require the exact knowledge of the measurement locations whose positions may be compromised by drift. We obtain the linear drift vector $\vec{d}$ by comparing topographic images before and after QPI mapping. Conveniently, the TSP measurement sequence imposes an exact timing for when each LDOS data point has been recorded. From the time difference between two sequential measurements $\Delta t = t_{i+1} - t_i$ and the total QPI mapping time $t = \sum_{i=1}^{N} t_i$, we correct the

respective LDOS coordinate $\vec{r}$ as $\vec{r}_c = \vec{r} - \vec{d}\Delta t/t$. Figure 4 exemplifies the working and impact of drift correction on our CS method. A comparison of the QPI patterns with and without drift correction shows a much clearer QPI recovery for the corrected TSP path, highlighted by a properly refocused surface-state wave vector and visible higher-order Bragg peaks.

V. CONCLUSION AND OUTLOOK

In conclusion, we have introduced an efficient sparse sampling method for quasiparticle interference mapping with the STM. Our method requires no additional hardware and can readily enhance the operation of existing STM facilities. The fundamental time savings of our method allows QPI experiments that go beyond the limits of conventional QPI mapping; our method enables the exploration of an exceedingly large parameter space for the characterization of advanced quantum materials or to invest the time savings in order to achieve unprecedented momentum space resolution. The suggested informed sampling variant provides further enhancement by either concentrating the random sampling around strong scatterers, by deliberately avoiding regions that would be discarded in conventional sampling after the fact, or by creating TSP-based sampling windows that mitigate Fourier artifacts. Our traveling salesman's approach for optimizing the path length of the STM tip significantly reduces additional measurement overhead and enables a straightforward drift correction. An interesting side effect of the known time sequence of the TSP is the possibility for a very precise characterization of periodic instrument noise (line noise and mechanical vibrations), whose frequencies are incoherently sampled during the TSP motion and that could then be removed using the CS recovery.

We recommend usual best practices in the preparation of a CS enhanced QPI mapping. These include the inspection of spectral features from point spectra to assess energy range and required voltage increments, the topographic labeling of strong scattering sites or no-go zones for an eventual informed sampling variant, and the initial exploration of topography, preferably with closed-loop dI/dV mapping to quantify the sparsity of the FFT domain, while keeping the inequality of Appendix A in mind.

As a perspective for future developments, we anticipate the inclusion of known crystal symmetries as additional constraints at the level of the CS recovery procedure. This could work by identifying the unit cell motives in the real-space/LDOS image, which would then serve as individual reference frames for the contained LDOS measurements and onto which the symmetry operations (mirror, rotation, translation, and combinations thereof) are applied. In consequence, the measurement matrix A would grow, which may allow us to further reduce the minimal number of required LDOS measurements. In contrast to *a posteriori* symmetrization, occasionally carried out in conventional QPI mapping, and which involves the averaging of the QPI pattern with their rotated/reflected copies, the CS based symmetry constraints might be less prone to artifacts [38] and allow for the consideration of more symmetry constraints, such as glide planes that are lost in the Fourier transform of the conventional method.

ACKNOWLEDGMENTS

F.D.N. appreciates support from the Swiss National Science Foundation under Project No. PP00P2_176866. We thank T. Greber, G. Genovese, and V. Madhavan for fruitful discussions. We also thank D. Walkup, J. Hoffman, M. Steinbrecher, and M. Allan for providing us with actual QPI datasets for the testing of our recovery method. The comparison of the fully sampled LDOS with the sparsely recovered QPI of those experimental datasets is available upon reasonable request.

APPENDIX A: SIMULATION DETAILS

In order to use our compressed sensing method for quasiparticle interference mapping we proceed as follows: We first generate a sampling matrix on a grid G of size $N = n \times n$ that is used to define the spatial locations of LDOS measurements. Depending on our sampling variant (random-point sampling or informed sampling), we exclude regions or favor entries that we randomly set to "1" for a fraction p of the entries, while the other $1 - p$ remain "0". The matrix G is thus a binary matrix, encoding the measurement locations at which we record the LDOS during our sparse mapping. We next compute a near-optimal solution to the open TSP connecting the just determined LDOS locations on G using a genetic algorithm [37]. Since the TSP is NP hard, the calculation of an optimal path for large sampling matrices may become cumbersome but a catalog of sampling masks could be calculated long before the actual QPI experiment for a range of p values and grid sizes N or the problem could be simplified by parallelly solving the TSP on subgrids that are later reconnected. The coordinates would next be fed in their optimal order to the STM controller for the sparse LDOS mapping, generating a measurement vector b of size $pN \times 1$. After recording the sparsely sampled LDOS, we subtract a global plane to bring the average LDOS to zero and next compute the QPI pattern using the Matlab based compressed sensing solver SPGL1 [39,40] and its basis pursuit denoising variant, which aims at minimizing $\|x\|_1$ subject to $\|Ax - b\|_2 \leqslant \sigma$. Here, x represents the s-sparse $N \times 1$ QPI pattern, A is the $pN \times N$ measurement matrix connecting real and momentum space, and σ is an adjustable noise tolerance threshold. Every row of A is calculated by letting the i^{th} nonzero entry of matrix G chose the i^{th} row of the $n \times n$ identity matrix onto which we apply the inverse Fourier transform. For instance, if the first and third entry of the G matrix were nonzero, the first two rows of matrix A would be composed of the inverse Fourier transform of the first and third row of the identity matrix. According to CS theory, successful recovery for such Fourier matrices is likely when $pN \geqslant Cs \ln^4(N)$, where $C > 0$ is a constant and s is the sparsity [36]. The sparsity s denotes here the number of nonzero pixels of the full QPI pattern. Note that we cast the $n \times n$ dimensional problem into a one-dimensional (1D) $N \times 1$ description, which we bring back to 2D after recovery and for illustration. The CS recovery directly yields the QPI pattern that we inverse Fourier transform to obtain the LDOS modulations in real space. For explorative closed-loop LDOS measurements at a fixed energy, a TSP or sparse line hopping

[41] could provide a fast overview of the QPI information using CS.

APPENDIX B: COMPRESSIVE SENSING RECOVERY ON ACTUAL LDOS DATA

We have tested our CS recovery method with previously published QPI data, using screenshots from available figures and notably the raw LDOS published in Refs. [24,25,29]. We find excellent CS recovery with only 40% of the samples for all cases and convincing recovery down to subsampling rates of 10–20% for Refs. [24,29]. A comparison of all three cases is available upon reasonable request addressed to F.D.N. Note that the strength of the joint DOS determines how much subsampling is required, which was the limiting factor for our trial on the data from Ref. [25], whose QPI pattern is more diffuse, meaning that the band details are described by more wave vectors in Fourier space, making this dataset less sparse. As a more general guide, we recommend scrutinizing the QPI pattern for its sparsity with the inequality of Appendix A in mind. This could be done with the help of a rapid closed-loop dI/dV mapping prior to a full CS investigation.

[1] B. Bradlyn, L. Elcoro, J. Cano, M. G. Vergniory, Z. Wang, C. Felser, M. I. Aroyo, and B. A. Bernevig, Topological quantum chemistry, Nature (London) **547**, 298 (2017).

[2] M. G. Vergniory, L. Elcoro, C. Felser, N. Regnault, B. A. Bernevig, and Z. Wang, A complete catalogue of high-quality topological materials, Nature (London) **566**, 480 (2019).

[3] A. R. Oganov, C. J. Pickard, Q. Zhu, and R. J. Needs, Structure prediction drives materials discovery, Nat. Rev. Mater. **4**, 331 (2019).

[4] M. Z. Hasan and C. L. Kane, Colloquium: Topological insulators, Rev. Mod. Phys. **82**, 3045 (2010).

[5] Y. Cao, V. Fatemi, S. Fang, K. Watanabe, T. Taniguchi, E. Kaxiras, and P. Jarillo-Herrero, Unconventional superconductivity in magic-angle graphene superlattices, Nature (London) **556**, 43 (2018).

[6] Y. Zhang, A. Mesaros, K. Fujita, S. D. Edkins, M. H. Hamidian, K. Ch'ng, H. Eisaki, S. Uchida, J. C. S. Davis, E. Khatami, and E.-A. Kim, Machine learning in electronic-quantum-matter imaging experiments, Nature (London) **570**, 484 (2019).

[7] A. Damascelli, Z. Hussain, and Z.-X. Shen, Angle-resolved photoemission studies of the cuprate superconductors, Rev. Mod. Phys. **75**, 473 (2003).

[8] M. Cattelan and N. A. Fox, A perspective on the application of spatially resolved ARPES for 2D materials, Nanomaterials **8**, 284 (2018).

[9] H. Yang, A. Liang, C. Chen, C. Zhang, N. B. M. Schroeter, and Y. Chen, Visualizing electronic structures of quantum materials by angle-resolved photoemission spectroscopy, Nat. Rev. Mater. **3**, 341 (2018).

[10] Y. J. Song, A. F. Otte, V. Shvarts, Z. Zhao, Y. Kuk, S. R. Blankenship, A. Band, F. M. Hess, and J. A. Stroscio, Invited Review Article: A 10 mK scanning probe microscopy facility, Rev. Sci. Instrum. **81**, 121101 (2010).

[11] T. Balashov, M. Meyer, and W. Wulfhekel, A compact ultrahigh vacuum scanning tunneling microscope with dilution refrigeration, Rev. Sci. Instrum. **89**, 113707 (2018).

[12] M. F. Crommie, C. P. Lutz, and D. M. Eigler, Imaging standing waves in a two-dimensional electron gas, Nature (London) **363**, 524 (1993).

[13] P. T. Sprunger, L. Petersen, E. W. Plummer, E. Lægsgaard, and F. Besenbacher, Giant Friedel oscillations on the beryllium(0001) surface, Science **275**, 1764 (1997).

[14] Ph. Hofmann, B. G. Briner, M. Doering, H.-P. Rust, E. W. Plummer, and A. M. Bradshaw, Anisotropic Two-Dimensional Friedel Oscillations, Phys. Rev. Lett. **79**, 265 (1997).

[15] L. Petersen, Ph. Hofmann, E. W. Plummer, and F. Besenbacher, Fourier transform-STM: Determining the surface Fermi contour, J. Electron Spectrosc. Relat. Phenom. **109**, 97 (2000).

[16] J. E. Hoffman, K. McElroy, D.-H. Lee, K. M. Lang, H. Eisaki, S. Uchida, and J. C. Davis, Imaging quasiparticle interference in $Bi_2Sr_2CaCu_2O_{8+\delta}$, Science **297**, 1148 (2002).

[17] S. Grothe, S. Johnston, S. Chi, P. Dosanjh, S. A. Burke, and Y. Pennec, Quantifying Many-Body Effects by High-Resolution Fourier Transform Scanning Tunneling Spectroscopy, Phys. Rev. Lett. **111**, 246804 (2013).

[18] E. W. Hudson, S. H. Pan, A. K. Gupta, K.-W. Ng, and J. C. Davis, Atomic-scale quasi-particle scattering resonances in $Bi_2Sr_2CaCu_2O_{8+\delta}$, Science **285**, 88 (1999).

[19] K. McElroy, R. W. Simmonds, J. E. Hoffman, D.-H. Lee, J. Orenstein, H. Eisaki, S. Uchida, and J. C. Davis, Relating atomic-scale electronic phenomena to wave-like quasiparticle states in superconducting $Bi_2Sr_2CaCu_2O_{8+\delta}$, Nature (London) **422**, 592 (2003).

[20] K. McElroy, D.-H. Lee, J. E. Hoffman, K. M. Lang, J. Lee, E. W. Hudson, H. Eisaki, S. Uchida, and J. C. Davis, Coincidence of Checkerboard Charge Order and Antinodal State Decoherence in Strongly Underdoped Superconducting $Bi_2Sr_2CaCu_2O_{8+\delta}$, Phys. Rev. Lett. **94**, 197005 (2005).

[21] T. Hanaguri, Y. Kohsaka, J. C. Davis, C. Lupien, I. Yamada, M. Azuma, M. Takano, K. Ohishi, M. Ono, and H. Takagi, Quasiparticle interference and superconducting gap in $Ca_{2-x}Na_xCuO_2Cl_2$, Nat. Phys. **3**, 865 (2007).

[22] M. J. Lawler, K. Fujita, J. Lee, A. R. Schmidt, Y. Kohsaka, C. K. Kim, H. Eisaki, S. Uchida, J. C. Davis, J. P. Sethna, and E.-A. Kim, Intra-unit-cell electronic nematicity of the high-T_c copper-oxide pseudogap states, Nature (London) **466**, 347 (2010).

[23] T.-M. Chuang, M. P. Allan, J. Lee, Y. Xie, N. Ni, S. L. Bud'ko, G. S. Boebinger, P. C. Canfield, and J. C. Davis, Nematic electronic structure in the "parent" state of the iron-based superconductor $Ca(Fe_{1-x}Co_x)_2As_2$, Science **327**, 181 (2010).

[24] M. Steinbrecher, H. Harutyunyan, C. R. Ast, and D. Wegner, Rashba-type spin splitting from interband scattering in quasiparticle interference maps, Phys. Rev. B **87**, 245436 (2013).

[25] Y. He, Y. Yin, M. Zech, A. Soumyanarayanan, M. M. Yee, T. Williams, M. C. Boyer, K. Chatterjee, W. D. Wise, I. Zeljkovic, T. Kondo, T. Takeuchi, H. Ikuta, P. Mistark, R. S. Markiewicz, A. Bansil, S. Sachdev, E. W. Hudson, and J. E. Hoffman, Fermi surface and pseudogap evolution in a cuprate superconductor, Science **344**, 608 (2014).

[26] K. Fujita, C. K. Kim, I. Lee, J. Lee, M. H. Hamidian, I. A. Firmo, S. Mukhopadhyay, H. Eisaki, S. Uchida, M. J. Lawler, E.-A. Kim, and J. C. Davis, Simultaneous transitions in cuprate momentum-space topology and electronic symmetry breaking, Science **344**, 612 (2014).

[27] E. P. Rosenthal, E. F. Andrade, C. J. Arguello, R. M. Fernandes, L. Y. Xing, X. C. Wang, C. Q. Jin, A. J. Millis, and A. N. Pasupathy, Visualization of electron nematicity and unidirectional antiferroic fluctuations at high temperatures in NaFeAs, Nat. Phys. **10**, 225 (2014).

[28] S. Jeon, B. B. Zhou, A. Gyenis, B. E. Feldman, I. Kimchi, A. C. Potter, Q. D. Gibson, R. J. Cava, A. Vishwanath, and A. Yazdani, Landau quantization and quasiparticle interference in the three-dimensional Dirac semimetal Cd_3As_2, Nat. Mater. **13**, 851 (2014).

[29] I. Zeljkovic, D. Walkup, B. A. Assaf, K. L. Scipioni, R. Sankar, F. Chou, and V. Madhavan, Strain engineering Dirac surface states in heteroepitaxial topological crystalline insulator thin films, Nat. Nanotechnol. **10**, 849 (2015).

[30] H. Inoue, A. Gyenis, Z. Wang, J. Li, S. W. Oh, S. Jiang, N. Ni, B. A. Bernevig, and A. Yazdani, Quasiparticle interference of the Fermi arcs and surface-bulk connectivity of a Weyl semimetal, Science **351**, 1184 (2016).

[31] R. Batabyal, N. Morali, N. Avraham, Y. Sun, M. Schmidt, C. Felser, A. Stern, B. Yan, and H. Beidenkopf, Visualizing weakly bound surface Fermi arcs and their correspondence to bulk Weyl fermions, Sci. Adv. **2**, e1600709 (2016).

[32] Z. Wang, D. Walkup, P. Derry, T. Scaffidi, M. Rak, S. Vig, A. Kogar, I. Zeljkovic, A. Husain, L. H. Santos, Y. Wang, A. Damascelli, Y. Maeno, P. Abbamonte, E. Fradkin, and V. Madhavan, Quasiparticle interference and strong electron-mode coupling in the quasi-one-dimensional bands of Sr_2RuO_4, Nat. Phys. **13**, 799 (2017).

[33] Y. Nakanishi-Ohno, M. Haze, Y. Yoshida, K. Hukushima, Y. Hasegawa, and M. Okada, Compressed sensing in scanning tunneling microscopy/spectroscopy for observation of quasi-particle interference, J. Phys. Soc. Jpn. **85**, 093702 (2016).

[34] D. L. Donoho, Compressed sensing, IEEE Trans. Inf. Theory **52**, 1289 (2006).

[35] E. J. Candès and J. K. Romberg, Tao, Terrence, Stable signal recovery from incomplete and inaccurate measurements, Commun. Pure Appl. Math. **59**, 1207 (2006).

[36] S. Foucart, H. Rauhut, *A Mathematical Introduction to Compressive Sensing*, Applied and Numerical Harmonic Analysis (Springer Science+Business Media, New York, 2013).

[37] J. Kirk, Open Traveling Salesman Problem–Genetic Algorithm (2014), available at https://www.mathworks.com/matlabcentral/fileexchange/21196.

[38] C. Mann, Commentary on the interpretation of Fourier-transform scanning tunneling microscopy data arXiv:1509.07807.

[39] E. van den Berg and M. P. Friedlander, SPGL1: A solver for large-scale sparse reconstruction (2019), https://friedlander.io/spgl1/.

[40] E. van den Berg and M. P. Friedlander, Probing the Pareto frontier for basis pursuit solutions, SIAM J. Sci. Comput. **31**, 890 (2008).

[41] L. Kovarik, A. Stevens, A. Liyu, and N. D. Browning, Implementing an accurate and rapid sparse sampling approach for low-dose atomic resolution STEM imaging, Appl. Phys. Lett. **109**, 164102 (2016).